Biodegradation behavior of magnesium and ZK60 alloy in artificial urine and rat models

Shiying Zhang [a, c, 1], Yanze Bi [b, c, 1], Jianye Li [a], Zhenguo Wang [b, c], Jingmin Yan [a], Jiawang Song [b, c], Haibo Sheng [a], Heqing Guo [a, **], Yan Li [b, d, *]

[a] Department of Urology, Air Force General Hospital, Beijing, China
[b] School of Materials Science and Engineering, Beihang University, Beijing 100191, China
[c] Key Laboratory of Aerospace Advanced Materials and Performance (Beihang University), Ministry of Education, Beijing 100191, China
[d] Beijing Key Laboratory for Advanced Functional Materials and Thin Film Technology (Beihang University), Beijing 100191, China

ABSTRACT

In this work, the biodegradable and histocompatibility properties of pure Mg and ZK60 alloy were investigated as new temporary implants for urinary applications. The corrosion mechanism in artificial urine was proposed using electrochemical impedance spectroscopy and potentiodynamic polarization tests. The corrosion potential of pure magnesium and ZK60 alloy were −1820 and −1561 mV, respectively, and the corrosion current densities were 59.66 ± 6.41 and 41.94 ± 0.53 μA cm^{-2}, respectively. The in vitro degradation rates for pure Mg and ZK60 alloy in artificial urine were 0.382 and 1.023 mm/y, respectively, determined from immersion tests. The ZK60 alloy degraded faster than the pure Mg in both artificial urine and in rat bladders (the implants of both samples are ø 3 mm × 5 mm). Histocompatibility evaluations showed good histocompatibility for the pure Mg and ZK60 alloy during the 3 weeks post-implantation in rat bladders, and no harm was observed in the bladder, liver and kidney tissues. The results provide key information on the degradation properties and corrosion mechanism of pure Mg and ZK60 alloy in the urinary system.

1. Introduction

Ureteral injury caused by either iatrogenic or traumatic reasons is one of the most important types of urinary system injury [1,2]. Ureteral injury usually leads to obstruction, hydronephrosis, renal damage, infection, urinary cysts and other urinary system complications, which seriously affect the quality of a patient's life [3—5]. After an operation, a ureteral injury is usually treated with a ureteral stent, which is placed in the repair site to maintain urinary tract patency and prevent ureteral restenosis [6,7]. Traditional ureteral stents are usually made by inert materials, e.g., stainless steel and polyurethane, which may cause long-term complications,

such as infection, pain, hematuria and the formation of capsids and stones. A second surgery is usually used to remove the stent, which may bring not only physical and psychological pain, but also the postoperative secondary infection to patients [8,9]. Therefore, it is of great clinical value to explore biodegradable ureteral stents to avoid requiring subsequent operations.

In recent years, some biodegradable polymers, such as alginate, gellan gum [10,11], PCL, PLGA [12] and PLCL [13] have been studied as potential materials for ureteral stents. However, it seems that a much longer degradation time (>6 months) and inadequate support for the urinary tract system are disadvantages for practical application. It is well known that magnesium and its alloys are promising candidates as degradable materials with high strength, low elastic modulus and good biocompatibility [14—17]. Although the Mg-Al-Zn and Mg-Y alloys have shown good corrosion behavior in artificial urine [18], the alloying elements Al and Y with doubtful biological safety may be harmful in ureteral stent applications. Many investigations have shown that the ZK60 (Mg-Zn-Zr) magnesium alloy exhibited good in vitro and in vivo degradation rates,

* Corresponding author. Department of Urology, Air Force General Hospital, 30 Fucheng road, Haidian distinct, Beijing 100142, China.
** Corresponding author. Department of Urology, Air Force General Hospital, 30 Fucheng road, Haidian distinct, Beijing 100142, China.
E-mail addresses: Guoheqing777@163.com (H. Guo), liyan@buaa.edu.cn (Y. Li).
Peer review under responsibility of KeAi Communications Co., Ltd.
[1] These two authors contributed equally to this article.

as well as excellent biocompatibility [19—22]. Moreover, ZK60 alloy possesses good mechanical properties with a uniform elongation of 10—30% and an ultimate tensile strength of 200—400 MPa, which make it suitable as an implantation material [23—25].

In our previous work, the in vitro and in vivo corrosion and histocompatibility of pure Mg and Mg-6Zn were studied in simulated body fluid (SBF) and with rats modeling [26]. The results indicated good histocompatibility of the Mg and the Mg-6Zn alloy in the bladder indwelling implantation. The aim of this study is to investigate the biodegradable properties of Mg and ZK60 alloys in artificial urine (AU) and in vivo conditions to provide guidelines for developing next generation ureteral stents.

2. Materials and methods

2.1. Sample preparation

Commercially available pure Mg (99.9%) and ZK60 alloy (Mg-5.6 wt % Zn-0.5 wt % Zr) ingots were used in this work. Both pure Mg and ZK60 samples were cut into 10 mm × 10 mm × 2 mm plates for the in vitro experiments. Cylinders of both pure Mg and ZK60 alloy with a uniform size of ø 3 mm × 5 mm were used for in vivo implantation. Prior to the experiments, the samples were successively ground with 200—5000 grit SiC abrasive papers, ultrasonically cleaned in absolute ethanol and then dried in air.

2.2. Microstructural characterization

The phase composition of the samples was identified using an X-ray diffractometer (XRD, Rigaku D/Max 2500) with Cu kα radiation at a scan rate of $5° \cdot min^{-1}$ in the 2θ range of 10—80°. Scanning electron microscopy (SEM, Quanta 200F) was used to observe the surface morphology, and an energy dispersive X-ray spectroscopy (EDS) attachment was employed to analyze the chemical compositions.

2.3. In vitro corrosion tests

2.3.1. Electrochemical measurements

The electrochemical measurements were conducted on a CHI-660e electrochemical workstation (CH Instruments, Inc., Shanghai) using the conventional three-electrode system to assess the corrosion behavior of pure Mg and ZK60 alloy in AU at 37 °C. The artificial urine (pH 5.8) was prepared according to the work described by Sónia [27], with $CaCl_2$ (0.65 g L^{-1}), $MgCl_2$ (0.65 g L^{-1}), NaCl (4.6 g L^{-1}), Na_2SO_4 (2.3 g L^{-1}), $Na_3C_3H_5O(CO_2)_3$ (0.65 g L^{-1}), $Na_2C_2O_4$ (0.02 g L^{-1}), KH_2PO_4 (2.8 g L^{-1}), KCl (1.6 g L^{-1}), NH_4Cl (1.0 g L^{-1}), urea (25.0 g L^{-1}), creatinine (1.1 g L^{-1}) and dextrose (0.3%). The saturated calomel electrode (SCE), graphite rods and samples acted as the reference, counter and working electrodes, respectively. The change in the open circuit potential (OCP) over time were directly tested by the electrochemical workstation. Prior to electrochemical impedance spectroscopy (EIS), the samples were immersed in the solution for 5 min and EIS was then carried out at the open circuit potential with a 5 mV amplitude signal from 10 kHz to 10 mHz. Potentiodynamic polarization was performed on samples at a scanning rate of 1 mV/s from −500 mV and 500 mV with respect to the OCP. The corrosion current density of each sample was extrapolated from the cathodic branch of the polarization curves [28]. An average of six samples was used for each test in each group.

2.3.2. Immersion tests

To further investigate the corrosion characteristics of the pure Mg and the ZK60 alloy samples, immersion tests were carried out in AU at 37 °C to monitor the pH variations in the AU and the mass losses of the samples according to the ASTM-G31-72 standard [29]. The ratio of surface area to solution volume was 0.20 ml mm^{-2}. The pH of AU was recorded using a PHB-4 pH meter (INESA Scientific Instrument, Co. Ltd., Shanghai) over an immersion time of 28 days. After various immersion times, the samples were removed from the solution, gently rinsed with ultrapure water and dried at room temperature. The corroded surface morphologies and compositions were determined by SEM and XRD. Then, the corrosion products were completely removed with 200 g L^{-1} chromic acid to measure the mass losses of the samples. An average of three samples were used for immersion tests in each time point.

2.4. In vivo histocompatibility evaluation

2.4.1. Animals

Wistar rats (8 weeks old, male, n = 6) were purchased from the Vital River company (Beijing, China) weighing between 300 g and 330 g. The rats were raised in appropriate cages (<5/cage) and adaptation under temperature-controlled conditions with a 12 h light/dark cycle and ad libitum access to water and food. The rats were randomly divided into two groups (n = 3, each group) according to the implant materials, Mg or ZK60 alloy. All the rats were treated according to the ethical principles of laboratory animal care. In this study, the usage of animals was approved by the Research Ethics Committee, Air Force General Hospital, China.

2.4.2. Surgical procedure

After weighing, 1% sodium pentobarbital (60 mg kg^{-1}) was used to anesthetize the rats. After anesthesia, the rats were fixed in a supine position on a constantly heated plate (37 °C). Then, 75% alcohol was used for the sterile procedures. Surgical procedures were performed using an operation microscope (Olympus, Japan). A middle abdominal incision (3 cm) was made and peritoneum was cut to expose the bladder. The urine was drained using a sterile syringe. Then, an incision (5 mm) was made on the apex of the bladder well, and the bladder was washed with normal saline. Interrupted suturing was performed to close the bladder. Afterwards, peritoneal lavage was performed using 50 U/ml penicillin and 50 μg/ml streptomycin. Finally, layer-by-layer suture was performed using a 4-0 non-absorbable suture.

2.4.3. Specimen collection and histopathological evaluation

After anesthesia, a middle abdominal incision was performed (6 cm) to expose the bladder, left kidney and liver. The bladder, left kidney and median lobe of liver were cut down and fixed in 10% neutral formalin for 72 h. After all the specimens were collected, the rats were euthanized using deep anesthesia. The samples taken from the bladder were ultrasonically cleaned by ethanol and dried in air. The surface morphology and corrosion products were analyzed by SEM and EDS attachment.

After being fixed in the 10% neutral buffered formalin solution for 72 h, the tissues obtained from the bladder, liver and kidney were washed with running water and dehydrated with ethanol. Then, the specimens were placed into xylene to obtain transparency and embedded in paraffin. Afterwards, the embedded tissues were cut into sections (4 μm thick) and stained with hematoxylin/eosin. The sections were dehydrated in absolute alcohol and rehydrated in water. They were then immersed in hematoxylin dye for 4 min, washed with water, differentiated in 70% alcohol and stained in 0.01% eosin for 5 s. Finally, the samples were immersed in 95% ethanol, dehydrated with absolute ethanol, and washed with xylene for 5 min. The histopathological examinations were performed by a pathologist using blind study groups. The assessed biologic response parameters included acute

inflammatory changes (induction of neutrophils), chronic inflammatory changes (induction of lymphocytes and plasma cells), fibrosis and foreign body reactions. Tissue reactions for the various parameters analyzed were scored as no, mild, moderate and marked levels.

2.5. Statistical analysis

SPSS statistics version 18 was used for data transformation and statistical analysis. Any significant difference was determined by the T-Test, the plotted data in the graphs represent mean (average) ± SD (standard deviation). A statistically significant difference was considered at $p < 0.05$.

3. Results

3.1. Microstructural characterization

Fig. 1 shows the XRD patterns of pure Mg and ZK60 alloy, before and after immersion in AU at 37 °C for 5 days. Pure Mg is composed of a single α-Mg matrix phase with lattice parameters of a = 0.32089 nm and c = 0.52106 nm [30,31]. The α-Mg phase and $MgZn_2$ second phases can be detected in the ZK60 alloy sample [32]. For the Mg-AU and ZK60-AU samples, some additional peaks appear in the XRD patterns. According to the EDS results shown in Fig. 5(g and h), these peaks are confirmed to correspond to the $Mg_3(PO_4)_2$ and $Mg_2P_2O_7$ phases on the surface of the pure Mg and ZK60 alloy that form after immersing in AU for 5 days.

3.2. In vitro corrosion properties

3.2.1. Electrochemical measurements

The OCP values of pure Mg and the ZK60 alloy monitored for 3600 s after immersion in AU at 37 °C are shown in Fig. 2(a). During the initial 750 s of immersion in the AU, both the OCP of the pure magnesium and the ZK60 alloy increase rapidly. The potential of the pure Mg changes from −1686 to −1658 mV vs. SCE, whereas that of the ZK60 shifts from −1610 to −1488 mV vs. SCE. However, after 750 s of immersion, the pure Mg and the ZK60 alloy exhibit different states over time. The OCP of the pure Mg increases in a stable manner, whereas the curve for the ZK60 alloy increases in a fluctuating manner. It is suggested that the OCP of the pure Mg and

Fig. 1. XRD patterns for the pure Mg and ZK60 alloy before and after immersion in the AU at 37 °C for 5 days.

the ZK60 alloy may take a further positive shift, and the potential shift of the pure Mg is likely to be larger than that of the ZK60 alloy after immersion in AU for longer times (>3600 s).

The potentiodynamic polarization curves (Tafel curves) for pure Mg and the ZK60 alloy in AU at 37 °C are shown in Fig. 2(b). The cathodic curve of the potentiodynamic polarization test represents the hydrogen evolution reaction, whereas the anodic curve indicates the dissolution of the working electrode. The corresponding corrosion potential (E_{corr}) and corrosion current density (i_{corr}) determined by Tafel extrapolation of the cathodic polarization curves are listed in Table 1. The E_{corr} and i_{corr} of the pure Mg are −1820 mV and 59.66 ± 6.41 µA cm^{-2}, respectively. The ZK60 alloy displayed a higher E_{corr} and lower i_{corr} compared with the pure Mg. This means that the ZK60 alloy possesses a higher corrosion potential and lower corrosion rate at the beginning of the AU immersion process than the pure Mg.

EIS was performed to obtain insights into the corrosion processes of the pure Mg and ZK60 alloy samples. The Nyquist and Bode plots for the pure Mg and ZK60 alloy samples immersed in AU are shown in Fig. 3(a)-(c). The Nyquist plots for the pure Mg and ZK60 alloy exhibit three semicircles corresponding to three time constants. The pure Mg sample exhibits larger capacitive loops at the high, medium and low frequencies, suggesting better corrosion resistance than ZK60 alloy. An electrical equivalent circuit with three time constants shown in Fig. 3(d) is used to fit the experimental EIS data with an inductive arc. The variable R_s corresponds to the solution resistance between the reference electrode and sample, CPE_1 is the capacitance of the corrosion products, and R_1 is the corresponding resistance, which is closely related to the thickness and defects of the corrosion products, especially the number of pores [33]. CPE_2 represents the double layer capacitance at the electrolyte/substrate surface, R_2 represents the relevant charge transfer resistance and L is due to the transfer and diffusion of charge. The electrical equivalent circuits reveal good fits in the Nyquist and Bode plots, and the fitted results are listed in Table 2. In AU, the pure Mg sample shows a large increase in R_1 (from 237.6 Ω cm^2 to 61.53 Ω cm^2) and R_2 (476.2 Ω cm^2 to 356.5 Ω cm^2) along with smaller CPE_1 and CPE_2 values. This means that the corrosion of the pure Mg sample is mitigated in the AU. The ZK60 alloy has a smaller R_1, R_2 and L due to the loose and porous corrosion layer on the surface, which is unable to protect the substrate against the corrosive medium as effectively.

The Bode impedance and phase angle plots for the pure Mg and the ZK60 alloy samples acquired in AU in Fig. 3(b) and (c) provide anti-corrosion information from different views. Pure Mg exhibits a larger impedance and phase angle over a wide range of frequencies compared to the ZK60 alloy samples. The impedance of the pure Mg at the low frequency of 10 mHz increases from 617 Ω cm^2 to (ZK60) 358 Ω cm^2, the maximum phase angle of the ZK60 is 60.1°, which increases to 68.8° in pure Mg immersed in AU.

3.2.2. Immersion tests

The mass loss and pH variations of the AU during the immersion tests for pure Mg and ZK60 alloy at 37 °C are shown in Fig. 4. Fig. 4(a) shows that the mass loss from both the pure Mg and ZK60 alloy increase linearly during the initial 24 h immersion. The pure Mg exhibits a very slow mass loss throughout the further immersion test over 28 days. However, the ZK60 alloy exhibits a larger weight loss rate (14.32 ± 0.18 mg cm^{-2}) than the pure Mg (5.11 ± 0.14 mg cm^{-2}). In Fig. 4(b), the pH value increases gradually from 5.80 to 7.47 for pure Mg and to 10.22 for the ZK60 alloy after 28 days of immersion. These results indicate that ZK60 possesses a faster degradable rate in AU than pure Mg, which is consistent with the potentiodynamic polarization and EIS results shown in Figs. 2 and 3, respectively.
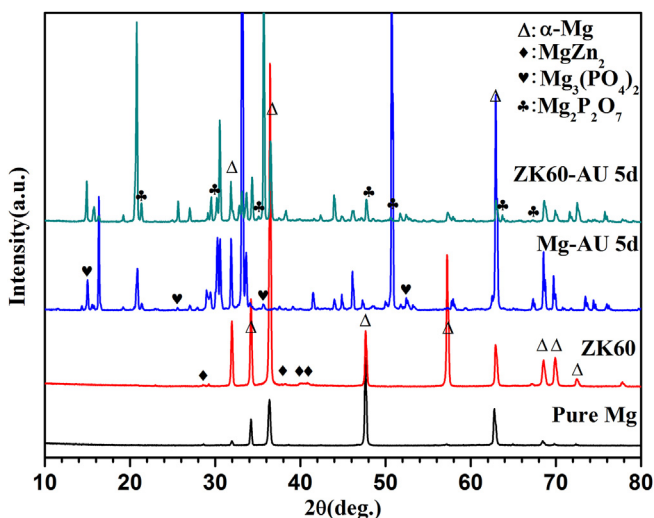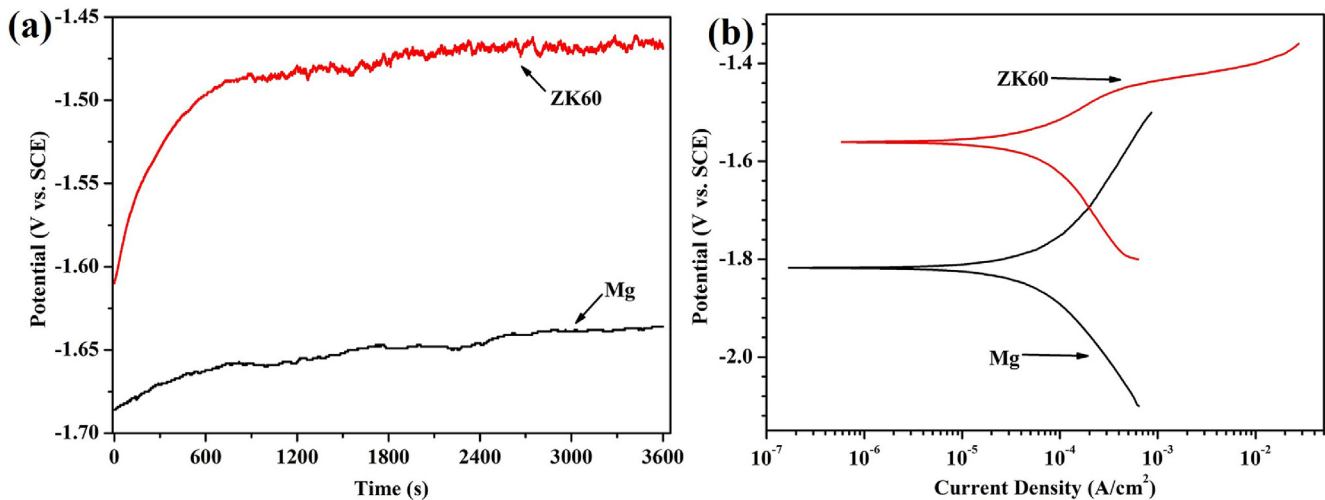
Fig. 2. (a) OCP curve and (b) potentiodynamic polarization curves for the pure Mg and ZK60 alloy in AU at 37 °C.

Fig. 5 shows the surface morphologies of the pure Mg and ZK60 alloy samples after the immersion tests in AU for 12 h, 24 h and 5 days when observed using SEM. The corrosion spreads rapidly across the entire surface of both the pure Mg and ZK60 alloy during immersion. At each immersion time, the ZK60 samples are observed to exhibit more severe corrosion than the pure Mg. After immersion for 12 h in AU, the pure Mg presents a completely corroded surface with cracks. These cracks act as channels for penetration of the corrosive solution, leading to the further dissolution of the metallic substrate. However, more loose corrosion products also cover the surface of the ZK60 alloy sample. After immersion for 48 h, the corrosion layer consists of outer and inner layer. Similar results have been obtained from corroded ZK60 and pure Mg soaked in SBF [34,35]. The fresh Mg substrate suffers from further attack and corrosion due to the penetration of the AU into and beyond the outer porous corrosion layer. As the immersion time increases, the corrosion products on the pure magnesium surface gradually thicken, but exhibit a relatively dense state. The ZK60 alloy surface corrosion products thicken in a similar fashion, but exhibit a looser state.

3.3. In vivo corrosion properties

Fig. 6 shows the surface morphologies and EDS results for the pure Mg and ZK60 alloy samples removed from the bladder after 3 weeks post-implantation. In Fig. 6(a), uniform corrosion products are seen to cover the surface of the pure Mg after 1 week post-implantation. The EDS results of zone G reveal that the precipitate is mainly composed of P and O, with a small amount of K and Mg (see Fig. 6(g)). For the same post-implantation time, the surface of the ZK60 alloy is severely corroded by the urine, and the precipitates exhibit two different morphologies: a flower-like shape and a block-like shape (indicated by H), as shown in Fig. 6(d). The EDS results in Fig. 6(h) indicate that the block-like shape consists of 15.38 C, 31.59 O, 18.08 Mg, 24.72 P and 10.23 K (in wt.%). After 2 weeks post-implantation in Fig. 6(b) and (e), both the pure Mg and

ZK60 alloy show the blocky precipitates on the surface becoming enlarged and getting thicker. At the end of 3 weeks post-implantation, the morphologies (Fig. 6(c) and (f)) of the two samples are still intact, but the crystalline deposition products on the pure Mg surface exhibit significant peeling. The main deposition products determined by EDS are MgO (Fig. 6(i)), and the surface deposition products of the ZK60 alloy are partially peeled off; however, a small amount of regular crystals can still be found. In our in vivo study, a large amount of urinary calculi was found to cover the surface of the ZK60 alloy sample implanted for 3 weeks, and the ZK60 sample was observed by SEM after removing the calculi. The urinary calculi significantly delayed the corrosion of the ZK60 sample. Therefore, the overall volume was relatively large compared to the pure Mg sample, as shown in Fig. 6(c).

3.4. Histological analyses

The HE-stained slices of the bladder, liver and kidney tissues are shown in Figs. 7—9, respectively, implanted with either the pure Mg or ZK60 alloy after 1 week, 2 weeks and 3 weeks post-implantation. No abnormal reaction was found in the samples (bladder (Fig. 7), liver (Fig. 8) and kidney (Fig. 9)). Moreover, there was no difference between the two groups at any time point. Thus, the bladder indwelling implantation test is stable and reliable. For the bladder, the mucous was smooth and without any mechanical damage, inflammatory reaction or other abnormal expressions. For the liver, there were no inflammatory manifestations or atrophy. Since the liver is the detoxification organ for the entire body, the materials proved to be non-toxic. When ureteral stents are set in the urinary system, one of the most common complications is retrograde infection. In the results from the renal samples, there was no inflammatory reaction or other abnormal signs. All these results suggest that the bladder indwelling model is safe and effective.

4. Discussion

4.1. Effect of alloying elements and artificial urine environment on the in vitro degradation properties

Comparing the XRD patterns of the pure Mg and ZK60 alloy in Fig. 1, second phases (e.g., $MgZn_2$) related to the alloying elements Zn and Zr are observed in the ZK60 alloy. According to the results from the electrochemical measurements shown in Fig. 2 and

Table 1
E_{corr} and i_{corr} of Mg and ZK60 in AU calculated from the cathodic polarization curves.

Samples	E_{corr} (mV vs. SCE)	i_{corr} ($\mu A/cm^2$)
Mg	−1820 ± 2	59.66 ± 6.41
ZK60	−1561 ± 8	41.94 ± 0.53
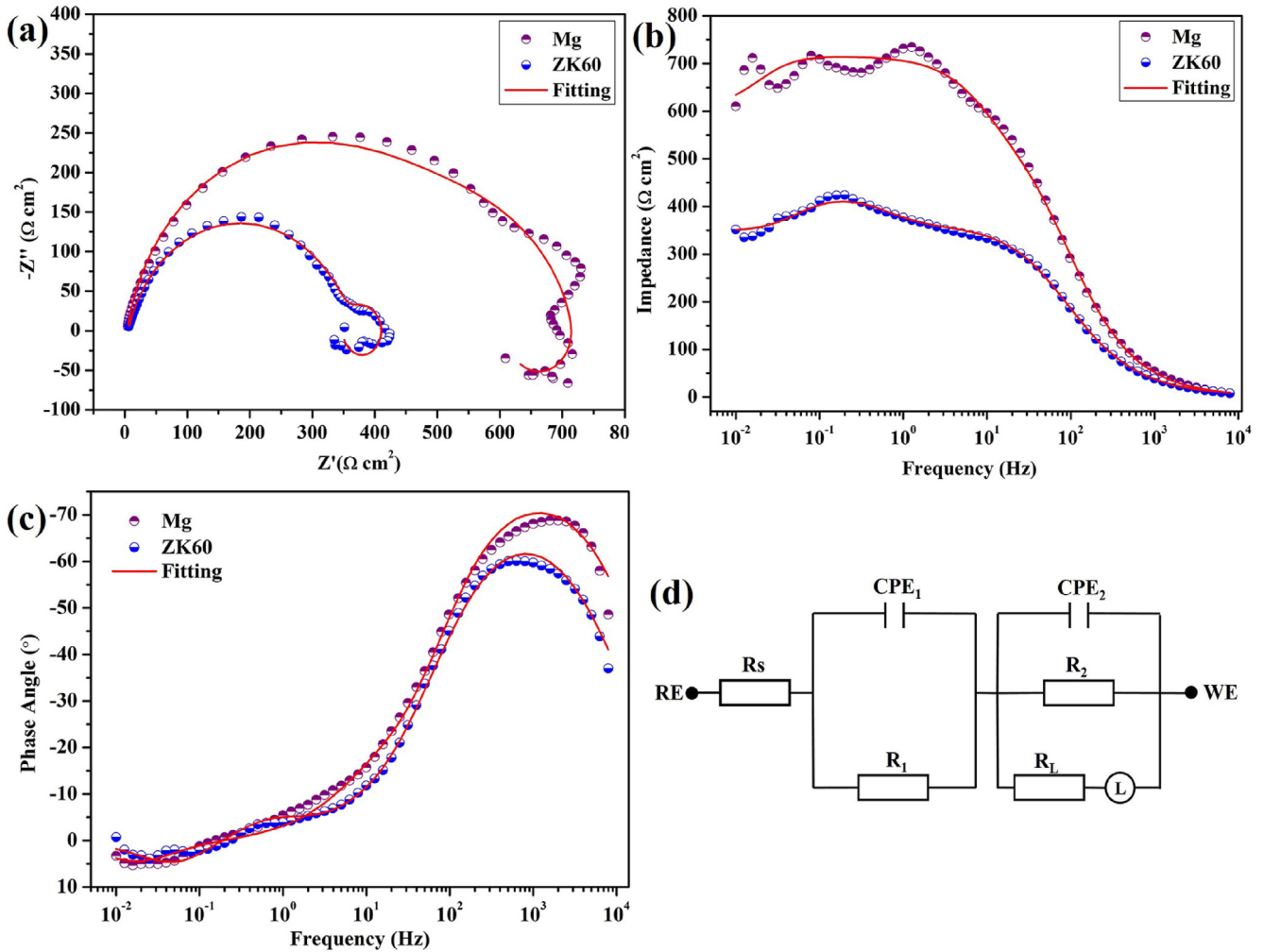
Fig. 3. (a) Nyquist, (b) Bode impedance and (c) phase angle plots monitored after 5 min of immersion, and (d) corresponding equivalent circuits for the pure Mg and ZK60 alloy in AU at 37 °C.

Table 1, the effect of Zn and Zr in ZK60 on corrosion behavior of the Mg can be summarized as follows: the Zn and Zr contribute to the decrease in i_{corr} and the increase in E_{corr} in the corrosion media, as shown in Refs. [36,37]. The $MgZn_2$ second phases cause a slowdown in the potential stability of the ZK60 alloy in the AU, as shown by the OCP testing (Fig. 2 (a)).

It is known that human urine exhibits acidic characteristics, as it contains a large amount of urea, uric acid and other inorganic salts [27]. The AU contains many special substances different from the SBF. For example, artificial urine contains urea, creatinine, and ten times more phosphate than SBF [38]. From the XRD patterns of the pure Mg and ZK60 alloy after immersion in AU at 37 °C for 5 days in Fig. 1, the long-term immersion corrosion products are mainly $Mg_3(PO_4)_2$ and $Mg_2P_2O_7$. These products are due to reactions (1)–(5), which are different from the corrosion products on the ZK60 alloy in SBF [35]. According to Lebouil's work [39], in AU, the phosphate ion (PO_4^{3-}), the hydrogen phosphate ion (HPO_4^{2-}), or the

dihydrogen phosphate ion ($H_2PO_4^-$) may transform into each other as the pH value varies. When the pH value of PBS is under 5.32, the states of Mg are Mg^{2+} and $Mg(H_2PO_4)^+$. The complex $Mg(HPO_4)_2$ compound appeared when the solution environment pH exceeded 5.32. As the pH increases, the complex $Mg(HPO_4)_2$ reacts to produce insoluble $Mg_3(PO_4)_2$. When the pH exceeds 7.0, the $Mg_3(PO_4)_2$ is gradually converted to soluble complex $MgPO_4$.

As seen in Fig. 4(a) and (b), when the pure Mg and ZK60 alloy samples are immersed in AU (initial pH = 5.8), the Mg materials dissolve following the reactions (1)–(4), and the pH of the AU increases rapidly. A large amount of insoluble $Mg_3(PO_4)_2$ (the corrosion products shown in Fig. 1) formed on the surface of the pure Mg and ZK60 via reaction (5). The microcell corrosion due to the second phase causes the ZK60 to dissolve faster than pure Mg, resulting in a pH increase rate that is higher than for pure Mg during the initial 12 h. According to the above analysis [39], a slightly higher pH in AU caused portions of the $Mg_3(PO_4)_2$ on ZK60 surfaces to dissolve.

Table 2
Fitted EIS results of Mg and ZK60 in AU based on the corresponding equivalent circuit models.

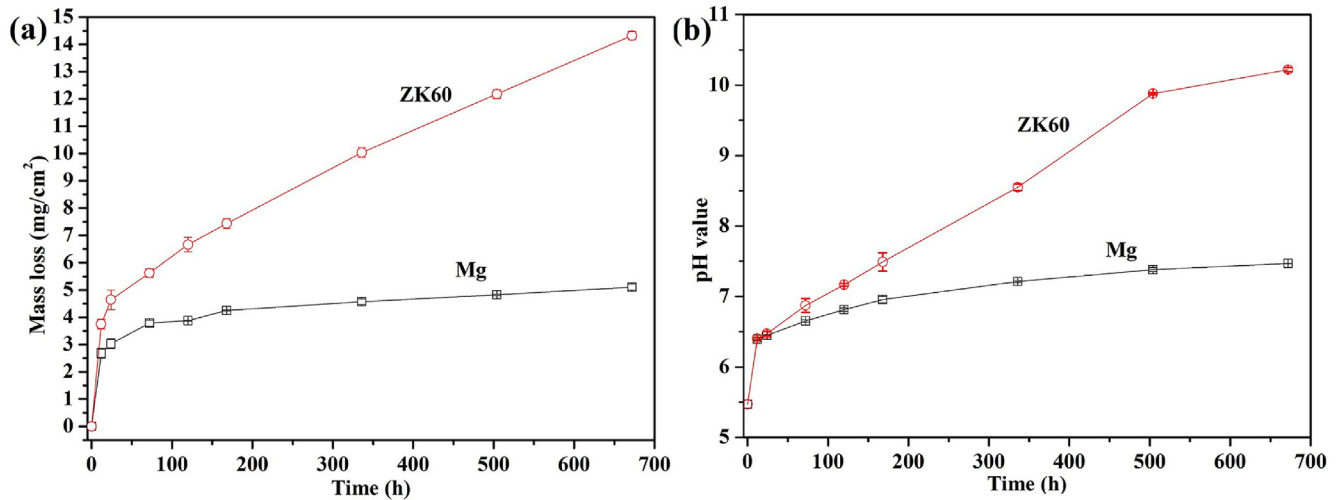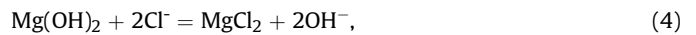| Samples	R_S (Ω cm^2)	CPE_1 (Ω^{-1} cm^{-2} s^{-n})	n_1	R_1 (Ω cm^2)	CPE_2 (Ω^{-1} cm^{-2} s^{-n})	n_2	R_2 (Ω cm^2)	L (H cm^2)
Mg	3.659	1.196×10^{-4}	0.8635	237.6	9.343×10^{-6}	0.8832	476.2	17370
ZK60	5.348	4.456×10^{-3}	0.9712	61.53	1.954×10^{-5}	0.8278	356.5	4757

Fig. 4. (a) Mass loss and (b) change in the pH of the AU for the pure Mg and ZK60 alloy immersed at 37 °C as a function of immersion time.

Therefore, the corrosion product layer on the ZK60 surface is less dense than on the pure Mg sample, and further exacerbated the corrosion of ZK60 alloy. After 5 days of immersion, the pH values for the pure Mg and ZK60 alloy were 6.81 ± 0.003 and 7.20 ± 0.002 (Fig. 4(b)), respectively. The pure Mg was covered by a dense corrosion product layer, whereas the ZK60 surface was covered with more porous corrosion products. The EDS results from areas G and H show that the corrosion products on the surface of pure Mg are close to $Mg_3(PO4)_2$, and the product composition on the surface of the ZK60 is close to $Mg_2P_2O_7$ (which is closer to the soluble complex) and that the porous structure is obtained by dissolving the $Mg_3(PO_4)_2$. Therefore, the mass loss and pH for the pure Mg samples increased more slowly than for the ZK60 alloy samples after 24 h of immersion:

$$Mg - 2e^- = Mg^{2+}, \tag{1}$$

$$2H_2O + 2e^- = 2OH^- + H_2, \tag{2}$$

$$Mg + 2H_2O = Mg(OH)_2 + H_2, \tag{3}$$

$$Mg(OH)_2 + 2Cl^- = MgCl_2 + 2OH^-, \tag{4}$$

$$3Mg^{2+} + 2PO_4^{3-} = Mg_3(PO_4)_2. \tag{5}$$

Based on the EIS tests shown in Fig. 3, a similar equivalent circuit has been used to explain the corrosion behavior of the ZK60 alloy [28], Mg-Sr, and Mg-Ca [40] in SBF. The larger R_1 and R_2 values for the pure Mg sample are attributed to the dense and stable corrosion product layer. The results show that the corrosion resistance of the pure Mg is better than that of the ZK60 in AU. The larger phase angle corresponds to a larger capacitive response, suggesting that the dense and stable surface provides good protection for the metallic substrate under the corrosive conditions [41]. The Bode impedance and phase angle results agree with those obtained from the Nyquist plots.

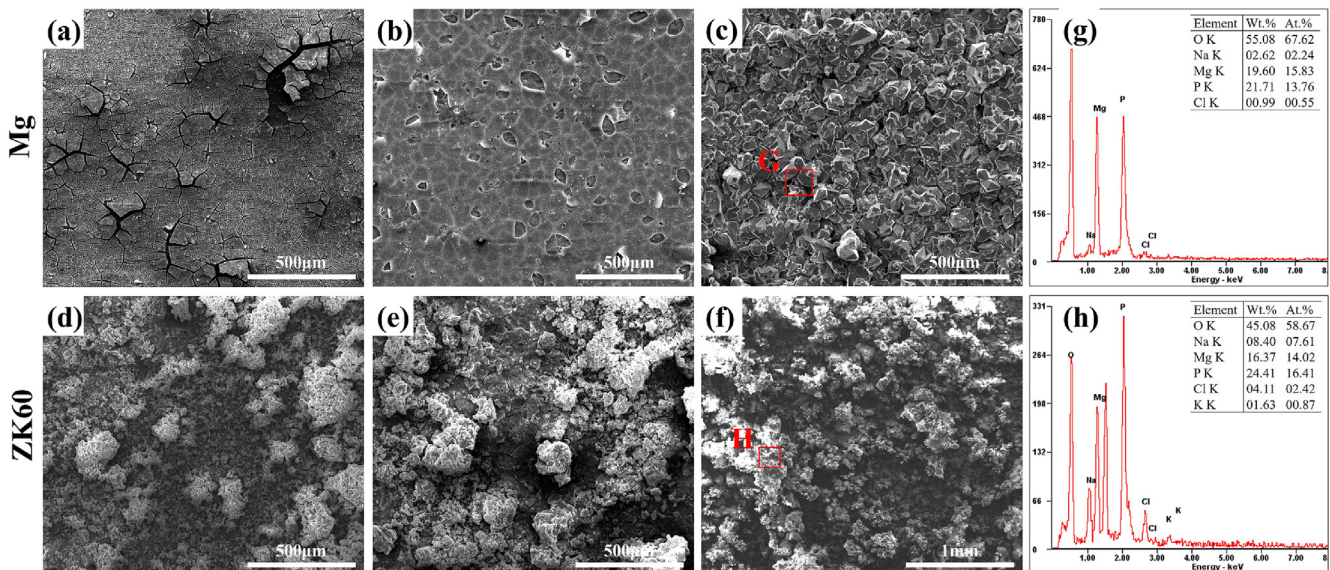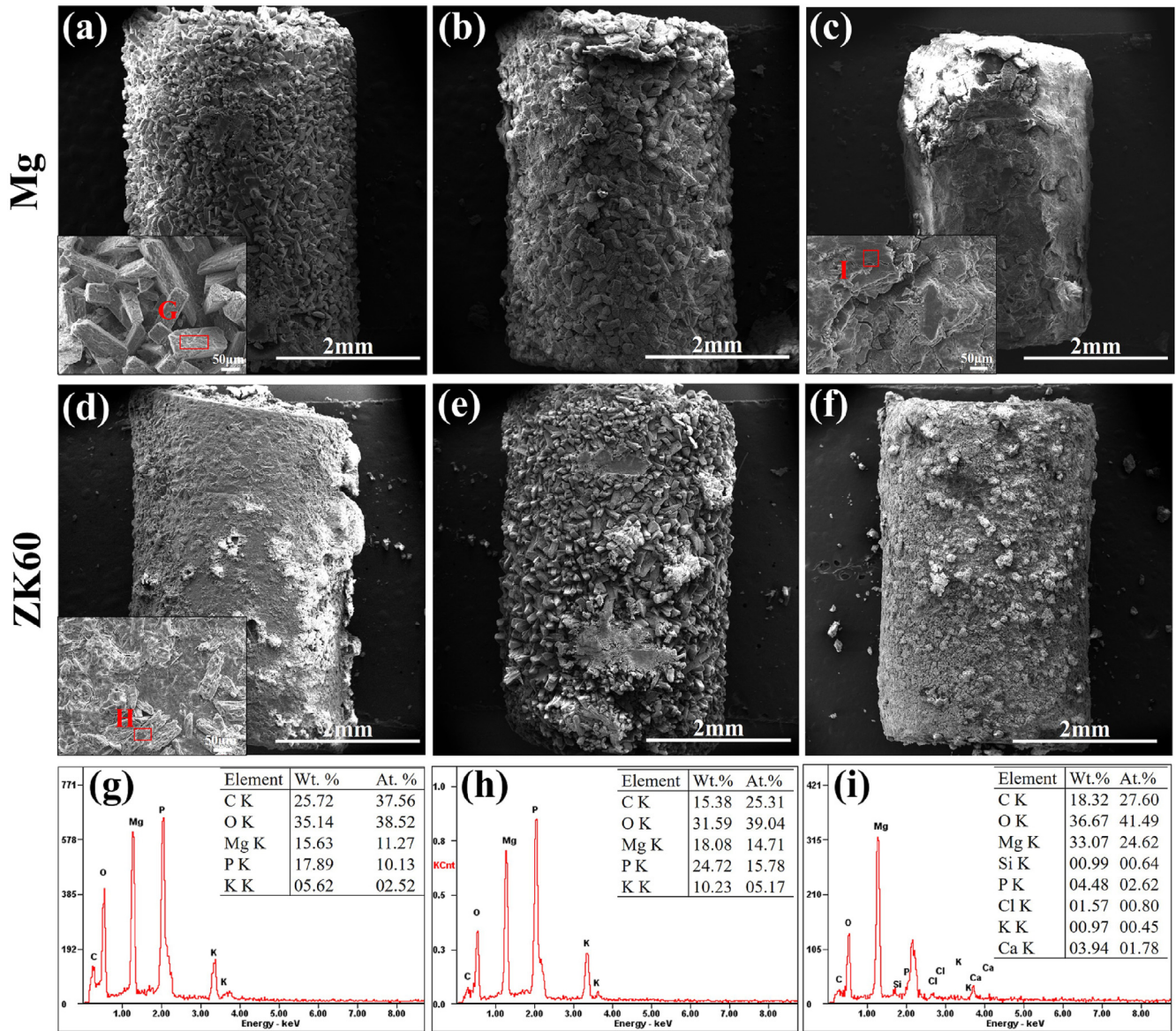Table 3 shows the corrosion rates for the pure Mg and ZK60 alloy

Fig. 5. Corroded surface morphologies and EDS results for the pure Mg after (a) 12 h, (b) 1 day and (b) 5 days and for the ZK60 alloy after (d) 12 h, (e) 1 day and (f) 5 days of immersion in AU at 37 °C.
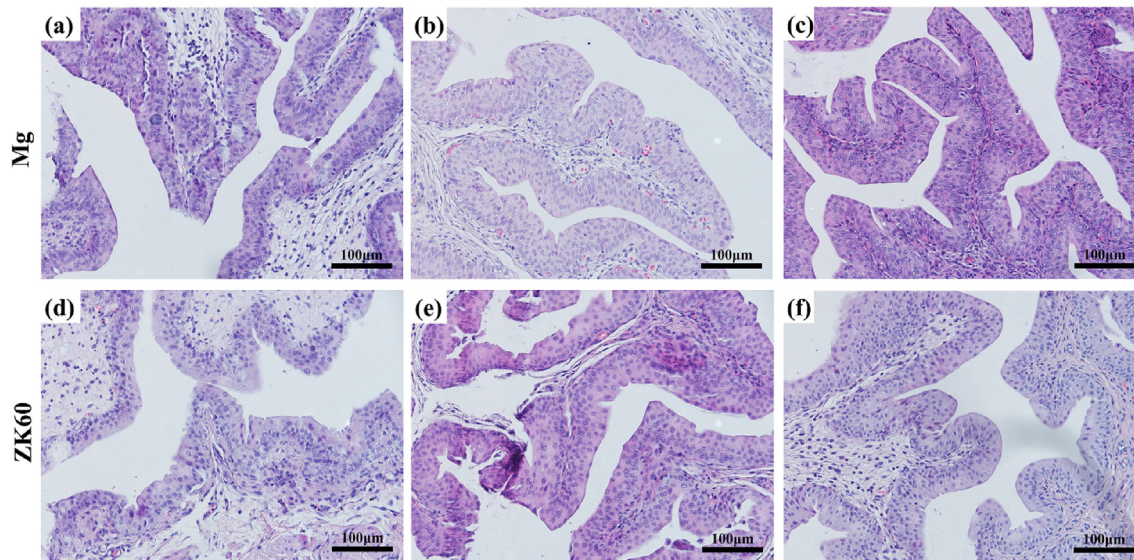
Fig. 6. Surface morphologies and EDS results for the pure Mg after: (a) 1 week, (b) 2 weeks and (c) 3 weeks post-implantation and for the ZK60 alloy after: (d) 1 week, (e) 2 weeks and (f) 3 weeks post-implantation. All the samples are removed from the rat bladders.

in AU at 37 °C obtained from the electrochemical measurements and immersion tests. We see from the Tafel extrapolation measurements that the corrosion rate of the ZK60 alloy ($P_i = 0.96 \pm 0.01$ mm/y) is lower than that of the pure Mg ($P_i = 1.36 \pm 0.14$ mm/y). However, a contrary result emerges from the immersion tests, with the ZK60 alloy presenting a corrosion rate of 1.023 ± 0.012 mm/y, suggesting a faster degradation than the pure Mg ($P_w = 0.382 \pm 0.013$ mm/y). This disagreement in corrosion rates between the two measurements has been reported in previous works [26,37,42] and may be ascribed to two aspects. First, the polarization measurements in Fig. 2(b) were carried out as short-term testing using 15 min immersion time. During the short-term testing, pure Mg corroded via reactions (1)–(3) and $Mg(OH)_2$ layer formed on the surface. For the ZK60 alloy, the oxidized Zn^{2+} reacted with the OH^- produced from reaction (2), resulting in not only $Mg(OH)_2$ but also zinc hydroxide ($Zn(OH)_2$) forming on the surface of the ZK60 alloy. The $Zn(OH)_2$ layer also decreased the corrosion current density over the short testing period. Second, the corrosion rate of ZK60 alloy was decreased by the $Zn(OH)_2$ layer

that formed during the initial period and was then accelerated by the Mg-Zn second phases as the zinc hydroxide layer gradually dissolved with increasing immersion time. The pure Mg offers more stable $Mg_3(PO_4)_2$ to achieve better corrosion resistance.

4.2. In vivo degradation and biocompatibility properties

Fig. 6 shows that after two weeks post-implantation, some magnesium phosphate deposition was observed on the samples, thickening the sediment. After 3 weeks post-implantation, the volume of pure magnesium is greatly reduced (Fig. 6(c)). This suggests that for longer-term implantations (3 weeks), the rat bladder has a certain extrusion and friction effect on the implanted samples, causing the magnesium phosphate deposited on the surface to be decreased and the degradation rate of the sample to accelerate. For the ZK60 alloy, some magnesium phosphate was deposited on the sample after 1 week implantation, whereas the phosphate compound formed on the sample after two weeks implantation. We note that the ZK60 sample retains its cylindrical

Fig. 7. HE-stained slices of the bladder tissues in contact with the pure Mg after: (a) 1 week, (b) 2 weeks and (c) 3 weeks post-implantation and the ZK60 alloy after: (d) 1 week, (e) 2 weeks and (f) 3 weeks post-implantation.

shape compared with pure Mg sample after 3 weeks implantation. This is due to the protection provided by the urinary calculi on the surface, which decrease the corrosion rate. Further research is needed to explore the inner mechanism.

4.3. Histological properties

Inflammation, proliferation and remodeling are the three sequential phases that occur during the healing process [43,44]. After the biodegradable materials were implanted in the organism, the implantation mainly affects the inflammation stage, which is considered a critical period for healing. During the entire implantation period, the reaction caused by implantation is a type of foreign body reaction. The biocompatibility and biodegradation of the material mainly determines the extent and duration of the inflammatory response after implantation. According to Figs. 7–9,

the urethral epithelial cells are smooth and packed closely, the liver cells do not exhibit any pathological changes, and the morphology and function of kidney cells and glomerular show no signs of lesions. Both the pure Mg and ZK60 alloy had no significant influence on the bladder, liver and kidney in the bladder implantation model, demonstrating excellent histocompatibility during the 3 weeks post-implantation. There are no differences between the pure Mg and the ZK60 alloy groups at any time for all the test tissues (bladder, liver and kidney).

5. Conclusion

The biodegradable and histocompatibility properties of pure Mg and the ZK60 alloy were investigated as new temporary implants for urinary applications. The corrosion mechanism in artificial urine is proposed using EIS and potentiodynamic polarization tests. The
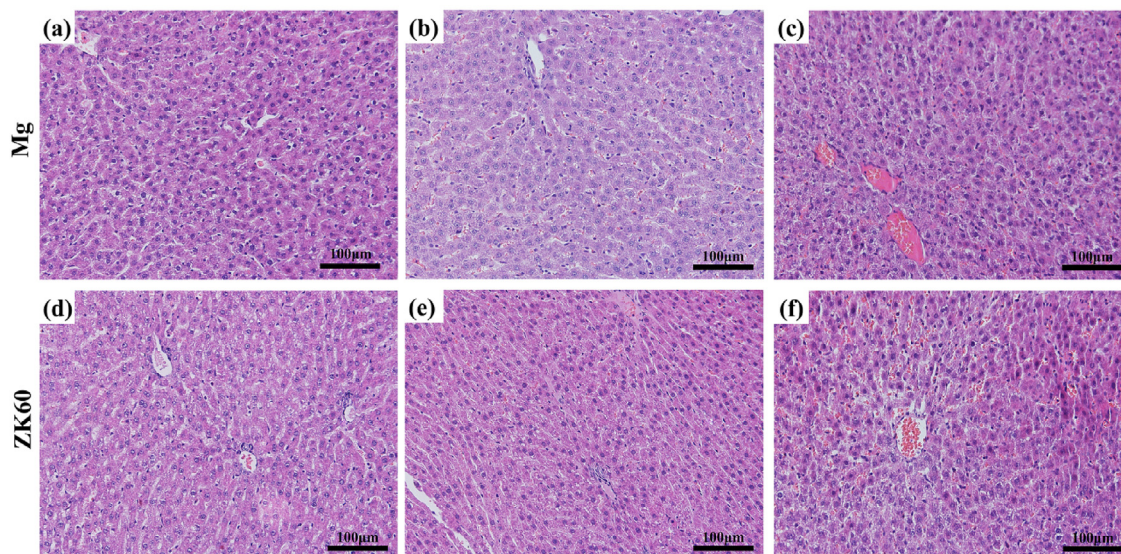
Fig. 8. HE-stained slices of the liver with the pure Mg implantation after: (a) 1 week, (b) 2 weeks and (c) 3 weeks post-implantation and the ZK60 alloy after: (d) 1 week, (e) 2 weeks and (f) 3 weeks post-implantation.
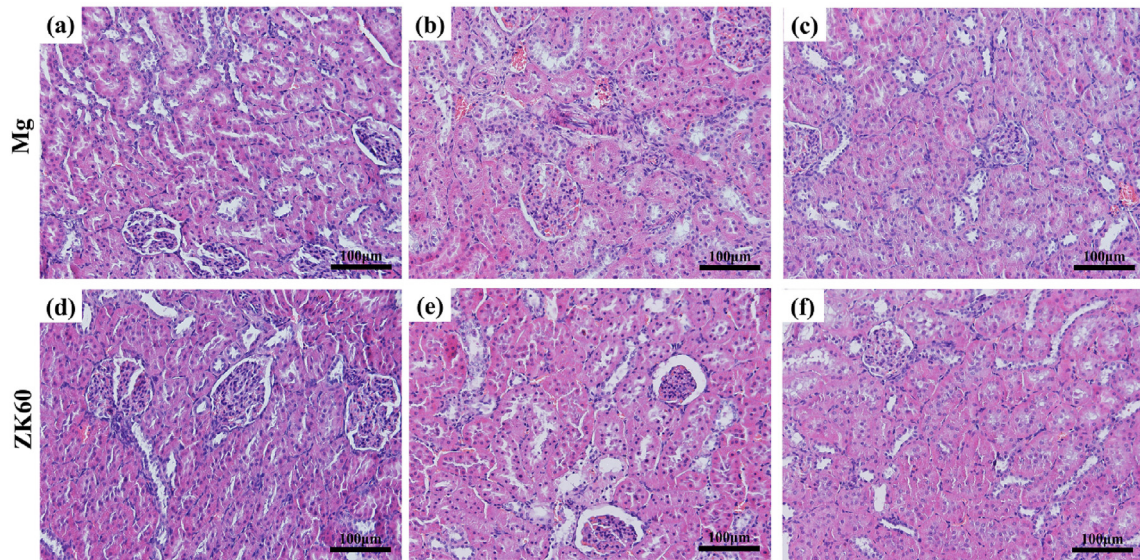
Fig. 9. HE-stained slices of the kidney with pure Mg implantation after (a) 1 week, (b) 2 weeks and (c) 3 weeks post-implantation and the ZK60 alloy after: (d) 1 week, (e) 2 weeks and (f) 3 weeks post-implantation.

Table 3
Corrosion rates of pure Mg and ZK60 alloy in AU at 37 °C calculated from electrochemical measurements (P_i) and immersion tests (P_w).

Samples	Electrochemical measurements		Immersion tests (28 days)	
	i_{corr} (μA/cm^2)	P_i (mm/y)	ΔW (mg/cm^2/d)	P_w (mm/y)
Mg	59.66 ± 6.41	1.36 ± 0.14	0.182 ± 0.006	0.382 ± 0.013
ZK60	41.94 ± 0.53	0.96 ± 0.01	0.511 ± 0.006	1.023 ± 0.012

corrosion potentials for pure Mg and ZK60 alloy are −1820 and 1561 mV, respectively, and the corrosion current densities are 59.66 ± 6.41 and 41.94 ± 0.53 μA cm^{-2}, the corrosion rates determined by current densities are 1.36 and 0.96 mm/y, respectively. The in vitro degradation rates for the pure Mg and ZK60 in artificial urine are 0.382 and 1.023 mm/y, respectively, as determined from the immersion tests. This difference related to the different stage of corrosion. The ZK60 alloy degraded faster than the pure Mg in both the artificial urine and the bladders of rats. Histocompatibility evaluations showed good histocompatibility for the pure Mg and ZK60 alloy during the 3 weeks post-implantation in the bladders of rats with no harm observed in the bladder, liver and kidney tissue. The results provide key information on the degradation properties and corrosion mechanism for pure Mg and ZK60 alloy in the urinary system, which is important to the potential development of Mg-based biodegradable stents for urinary applications.

References

[1] T.A.T. Marcelissen, P.P. Den Hollander, T.R.A.H. Tuytten, M.N. Sosef, Incidence of iatrogenic ureteral injury during open and laparoscopic colorectal surgery: a single center experience and review of the literature, Surg. Laparo. Endo. Per. 26 (2016) 513−515.
[2] S. Kawasaki, H. Shigematsu, H. Matsumori, N. Maegawa, Y. Tanaka, Ureteral injury as a possible complication of vertebral fracture in a patient with ankylosing spinal hyperostosis, J. Orthop. Sci. Off. J. Jpn. Orthop. Assoc. (2016), http://dx.doi.org/10.1016/j.jos.2016.05.012.
[3] V.T. Packiam, A.J. Cohen, J.J. Pariser, C.U. Nottingham, S.F. Faris, G.T. Bales, The impact of minimally invasive surgery on major iatrogenic ureteral injury and subsequent ureteral repair during hysterectomy: a national analysis of risk factors and outcomes, Urology 98 (2016) 183−188.
[4] A. Başer, O. Alkiş, C. Toktaş, A.E. Zümrütbaş, A rare cause of ureteral injuries; simultaneous common iliac artery and ureter injury during posterior lumbar disc surgery, Turkish J. Urol. 42 (2016) 108−110.
[5] Y. Xu, Q. Wang, F. Wang, Previous cesarean section and risk of urinary tract injury during laparoscopic hysterectomy: a meta-analysis, Int. Urogynecol. J. 26 (2015) 1269−1275.
[6] J. Fiuk, Y. Bao, J.G. Calleary, B.F. Schwartz, J.D. Denstedt, The use of internal stents in chronic ureteral obstruction, J. Urol. 193 (2015) 1092−1100.
[7] T. Kawahara, K. Sakamaki, H. Ito, S. Kuroda, H. Terao, K. Makiyama, H. Uemura, M. Yao, H. Miyamoto, J. Matsuzaki, Developing a preoperative predictive model for ureteral length for ureteral stent insertion, BMC Urol. 16 (2016) 70.
[8] M. Gultekinoglu, B. Kurum, S. Karahan, D. Kart, M. Sagiroglu, N. Ertas, A.H. Ozen, K. Ulubayram, Polyethyleneimine brushes effectively inhibit encrustation on polyurethane ureteral stents both in dynamic bioreactor and in vivo, Mat. Sci. Eng. C-Mater. 71 (2017) 1166−1174.
[9] M. Kim, B. Hong, H.K. Park, Long-term outcomes of double-layered poly-tetrafluoroethylene membrane-covered self-expandable segmental metallic stents (Uventa) in patients with chronic ureteral obstructions: is it really safe? J. Endourol. 30 (2016) 1339−1346.
[10] A.A. Barros, C. Oliveira, R.L. Reis, E. Lima, A. Rita, C. Duarte, Ketoprofen-eluting biodegradable ureteral stents by CO2 impregnation: in vitro study, Int. J. Pharm. 495 (2015) 651−659.
[11] A.A. Barros, A. Rita, C. Duarte, R.A. Pires, B.S. Marques, P. Ludovico, E. Lima, J.F. Mano, R.L. Reis, Bioresorbable ureteral stents from natural origin polymers, J. Biomed. Mater. Res. B 103B (2015) 608−617.
[12] X. Wang, H. Shan, J. Wang, Y. Hou, J. Ding, Q. Chen, J. Guan, C. Wang, X. Chen, Characterization of nanostructured ureteral stent with gradient degradation in a porcine model, Int. J. Nanomed. 10 (2015) 3055−3064.
[13] X.F. Ma, Y. Xiao, H. Xu, K. Lei, M.D. Lang, Preparation, degradation and in vitro release of ciprofloxacin-eluting ureteral stents for potential antibacterial application, Mater. Sci. Eng. C 66 (2016) 92−99.
[14] M.P. Staiger, A.M. Pietak, J. Huadmai, G. Dias, Magnesium and its alloys as orthopedic biomaterials: a review, Biomaterials 27 (2006) 1728−1734.
[15] Y.F. Zheng, X.N. Gu, F. Witte, Biodegradable metals, Mater. Sci. Eng. R. Rep. 77 (2014) 1−34.
[16] M. Haude, R. Erbel, P. Erne, S. Verheye, H. Degen, D. Bose, et al., Safety and performance of the drug-eluting absorbable metal scaffold (DREAMS) in patients with de-novo coronary lesions: 12 month results of the prospective, multicentre, first-in-man BIOSOLVE-I trial, Lancet 381 (2013) 836−844.
[17] N. Li, Y.F. Zheng, Novel magnesium alloys developed for biomedical application: a review, J. Mater. Sci. Technol. 29 (2013) 489−502.
[18] J.Y. Lock, E. Wyatt, S. Upadhyayula, A. Whall, V. Nuñez, V.I. Vullev, H.N. Liu, Degradation and antibacterial properties of magnesium alloys in artificial urine for potential resorbable ureteral stent applications, J. Biomed. Mater. Res. A 102A (2014) 781−792.

[19] Z.G. Huan, M.A. Leeflang, J. Zhou, L.E. Fratila-Apachitei, J. Duszczyk, In vitro degradation behavior and cytocompatibility of Mg—Zn—Zr alloys, J. Mater. Sci. Mater. Med. 21 (2010) 2623—2635.

[20] X.N. Gu, N. Li, Y.F. Zheng, L.Q. Ruan, In vitro degradation performance and biological response of a Mg-Zn-Zr alloy, Mater. Sci. Eng. B-Adv. 176 (2011) 1778—1784.

[21] Z.R. Qi, Q. Zhang, L.L. Tan, X. Lin, Y. Yin, X.L.K. Yang, Y. Wang, Comparison of degradation behavior and the associated bone response of ZK60 and PLLA in vivo, J. Biomed. Mater. Res. A 102 (2014) 1255—1263.

[22] X. Lin, L.L. Tan, Q. Wang, G.D. Zhang, B.C. Zhang, K. Yang, In vivo degradation and tissue compatibility of ZK60 magnesium alloy with micro-arc oxidation coating in a transcortical model, Mat. Sci. Eng. C-Mater. 33 (2013) 3881—3888.

[23] W.B. Yu, Z.Y. Liu, H. He, N.P. Cheng, X.L. Li, Microstructure and mechanical properties of ZK60-Yb magnesium alloys, Mater. Sci. Eng. A-Struct. Mater. 478 (2008) 101—107.

[24] H.T. Zhou, Z.D. Zhang, C.M. Liu, Q.W. Wang, Effect of Nd and Y on the microstructure and mechanical properties of ZK60 alloy, Mater. Sci. Eng. A-Struct. Mater. 445 (2007) 1—6.

[25] D. Orlov, G. Raab, T.T. Lamark, M. Popov, Y. Estrin, Improvement of mechanical properties of magnesium alloy ZK60 by integrated extrusion and equal channel angular pressing, Acta Mater. 59 (2011) 375—385.

[26] S.Y. Zhang, Y. Zheng, L.M. Zhang, Y.Z. Bi, J.Y. Li, J. Liu, Y.B. Yu, H.Q. Guo, Y. Li, In vitro and in vivo corrosion and histocompatibility of pure Mg and a Mg-6Zn alloy as urinary implants in rat model, Mat. Sci. Eng. C-Mater. 68 (2016) 414—422.

[27] S. Sónia, N. Melyssa, H. Mariana, O. Rosário, W. David, A. Joana, Silicone colonization by non-Candida albicans Candida species in the presence of urine, J. Med. Microbiol. 59 (2010) 747—754.

[28] M.I. Jamesh, G.S. Wu, Y. Zhao, D.R. McKenzie, M.M.M. Bilek, P.K. Chu, Effects of zirconium and oxygen plasma ion implantation on the corrosion behavior of ZK60 Mg alloy in simulated body fluids, Corros. Sci. 82 (2014) 7—26.

[29] American Society for Testing and Materials, ASTM-G31—72: standard practice for laboratory immersion corrosion testing of metals, in: Annual Book of ASTM Standards, ASTM, 2004.

[30] Y. Zheng, Y. Li, J.H. Chen, Z.Y. Zou, Effects of tensile and compressive deformation on corrosion behaviour of a Mg—Zn alloy, Corros. Sci. 90 (2015) 445—450.

[31] Y.Z. Bi, Y. Zheng, Y. Li, Microstructure and mechanical properties of sintered porous magnesium using polymethyl methacrylate as the space holder, Mater. Lett. 161 (2015) 583—586.

[32] S.M. He, L.M. Peng, X.Q. Zeng, W.J. Ding, Y.P. Zhu, Comparison of the microstructure and mechanical properties of a ZK60 alloy with and without 1.3 wt. % gadolinium addition, Mater. Sci. Eng. A-Struct. Mater. 433 (2006) 175—181.

[33] G.L. Song, Z. Shi, Corrosion mechanism and evaluation of anodized magnesium alloys, Corros. Sci. 85 (2014) 126—140.

[34] X. Zhang, X.W. Li, J.G. Li, X.D. Sun, Preparation and characterizations of bioglass ceramic cement/Ca-P coating on pure magnesium for biomedical applications, ACS Appl. Mater. Inter. 6 (2014) 513—525.

[35] M.I. Jamesh, G. Wu, Y. Zhao, D.R. McKenzie, M.M.M. Bilek, P.K. Chu, Electrochemical corrosion behavior of biodegradable Mg-Y-RE and Mg-Zn-Zr alloys in Ringer's solution and simulated body fluid, Corros. Sci. 91 (2015) 160—184.

[36] X. N Gu, Y.F. Zheng, Y. Cheng, S.P. Zhong, T.F. Xi, In vitro corrosion and biocompatibility of binary magnesium alloys, Biomaterials 30 (2009) 484—498.

[37] G.L. Song, A. Atrens, Understanding magnesium corrosion, Adv. Eng. Mater. 5 (2003) 837—858.

[38] T. Kokubo, H. Takadama, How useful is SBF in predicting in vivo bone bioactivity? Biomaterials 27 (2006) 2907—2915.

[39] S. Lebouil, O. Gharbi, P. Volovitch, K. Ogle, Mg dissolution in phosphate and chloride electrolytes: insight into the mechanism of the negative difference effect, Corrosion 71 (2015) 234—241.

[40] Y. Zhao, M.I. Jamesh, W.K. Li, G. Wu, C. Wang, Y. Zheng, K.W.K. Yeung, P.K. Chu, Enhanced antimicrobial properties, cytocompatibility, and corrosion resistance of plasma-modified biodegradable magnesium alloys, Acta Biomater. 10 (2014) 544—556.

[41] C. Liu, Q. Bi, A. Leyland, A. Matthews, An electrochemical impedance spectroscopy study of the corrosion behavior of PVD coated steels in 0.5 M NaCl aqueous solution: part II: EIS interpretation of corrosion behavior, Corros. Sci. 45 (2003) 1257—1273.

[42] H.Y. Ha, J.Y. Kang, J. Yang, C.D. Yim, B.S. You, Limitations in the use of the potentiodynamic polarization curves to investigate the effect of Zn on the corrosion behavior of as-extruded Mg-Zn binary alloy, Corros. Sci. 75 (2013) 426—433.

[43] D.M. Vasconcelos, S.G. Santos, M. Lamghari, M.A. Barbosa, The two faces of metal ions: from implants rejection to tissue repair/regeneration, Biomaterials 84 (2016) 262—275.

[44] P. Martin, Wound healing-aiming for perfect skin regeneration, Science 276 (1997) 75—81.